

<sup>1</sup> Differential response of a tree-killing bark beetle to host tree size  
<sup>2</sup> across a gradient of climatic water deficit

<sup>3</sup> Michael J. Koontz<sup>1,2,\*</sup>, Andrew M. Latimer<sup>1,2</sup>, Leif A. Mortenson<sup>3</sup>, Christopher J. Fettig<sup>3</sup>, Malcolm P.  
<sup>4</sup> North<sup>1,2,4</sup>

<sup>5</sup> <sup>1</sup>Graduate Group in Ecology, University of California, Davis, CA, USA

<sup>6</sup> <sup>2</sup>Department of Plant Sciences, University of California, Davis, CA, USA

<sup>7</sup> <sup>3</sup>USDA Forest Service, Pacific Southwest Research Station, Placerville, CA, USA

<sup>8</sup> <sup>4</sup>USDA Forest Service, Pacific Southwest Research Station, Davis, CA, USA

<sup>9</sup> \*Correspondence: michael.koontz@colorado.edu

<sup>10</sup> Date report generated: April 24, 2019

<sup>11</sup> **Abstract**

<sup>12</sup> The recent Californian hot drought of 2012 to 2015 created favorable conditions for unprecedented ponderosa  
<sup>13</sup> pine mortality in the driest, densest portions of the Sierra Nevada mountain range, largely caused by the  
<sup>14</sup> western pine beetle (*Dendroctonus brevicomis*). Climate conditions related to tree water stress as well as forest  
<sup>15</sup> structure can influence the severity of forest insect disturbance, but it remains challenging to consider how  
<sup>16</sup> these variables may interact to produce patterns of tree mortality. Previous studies have shown an interaction  
<sup>17</sup> between climate conditions and forest density in their effect on tree mortality, but density is a coarse gauge  
<sup>18</sup> of forest structure that can affect western pine beetle behavior in a number of ways. Measuring broad-scale  
<sup>19</sup> climate conditions simultaneously with complex forest structure— including tree species, tree size, and local  
<sup>20</sup> density— will refine our understanding of how these variables interact, but is generally expensive and/or  
<sup>21</sup> labor-intensive. We overcame these hurdles by using a small, unhumanned aerial system (hereafter ‘drone’)  
<sup>22</sup> to conduct aerial surveys over an established network of 32 forest plots along a 350km and 1000m elevation  
<sup>23</sup> gradient in western slope Sierra yellow pine/mixed-conifer forests. Using Structure from Motion (SfM)  
<sup>24</sup> processing on over 450,000 images and field measurements from the coincident ground plots, we determined  
<sup>25</sup> tree size, location, and species for individual trees over 9 square kilometers of forest that experienced ponderosa  
<sup>26</sup> pine mortality as a result of western pine beetle activity. We modeled the probability of ponderosa pine  
<sup>27</sup> mortality as a linear combination of forest structure variables and site-level climatic water deficit, and used a  
<sup>28</sup> Gaussian process to estimate the spatial covariance in the response.

<sup>29</sup> We found that greater host density strongly increased the probability of host mortality, and greater host

size generally decreased the probability of host mortality. There was also a strong three-way interaction between host density, host size, and climatic water deficit such that host density and host size tended to synergistically increase the probability of host mortality at hot/dry sites, but denser, smaller trees tended to drive mortality in cool/wet sites.

Our results demonstrate a variable response of the western pine beetle to complex forest structure across an environmental gradient during the same hot drought, which may indicate forest sites were in different stages of disturbance (from “endemic” to “outbreak”) depending on their regional climate. Management interventions that reduce stem density may decrease the severity of western pine beetle disturbance in the future, and our results suggest that focusing these treatments on areas that are most likely to exceed feedback thresholds (i.e., hot/dry sites with many available hosts) will have the best chance of increasing the survivorship probability of larger trees.

## Introduction

Aggressive bark beetles dealt the final blow to many of the nearly 150 million trees killed in the California hot drought of 2012 to 2015 and its aftermath (USDAFS 2019). A harbinger of climate change effects to come, record high temperatures exacerbated the drought (Griffin and Anchukaitis 2014), which increased water stress on trees (Asner et al. 2016), making them more susceptible to attacking bark beetles (Fettig 2012, Kolb et al. 2016). A century of fire suppression policy has enabled forests to grow into dense stands, which also makes them more vulnerable to bark beetle attack (Fettig 2012). This combination of environmental conditions and forest structural characteristics led to tree mortality events of unprecedented size in the driest, densest forests across the state (Young et al. 2017). The mechanisms underlying the link between tree susceptibility to insect attack and hot, dry conditions are often directly attributed to tree physiology (Bentz et al. 2010), while the link to forest density is multifaceted (Fettig 2012). Because forest density is a coarse metric of the complex forest structure to which bark beetles respond (Raffa et al. 2008), our understanding of the connection between forest density and insect disturbance severity could be enhanced with more finely-resolved measures of forest structure, such as tree size, tree species, and local density within a forest stand (Stephenson et al. 2019, Fettig et al. 2019). Further, the interaction between local-scale complex forest structure and broad-scale environmental conditions as they affect forest insect disturbance remains underexplored (Seidl et al. 2016, Stephenson et al. 2019, Fettig et al. 2019).

The yellow pine/mixed-conifer forests in California’s Sierra Nevada region are characterized by regular bark beetle disturbances, primarily by the western pine beetle (*Dendroctonus brevicomis*) and its main host in the system, ponderosa pine (*Pinus ponderosa*) (Fettig et al. 2019). The western pine beetle is a “primary”

61 or “aggressive” bark beetle, with reproductive success contingent upon enough beetles “mass attacking” the  
62 host tree, overwhelming its defenses, and causing mortality (Raffa and Berryman 1983, Fettig et al. 2019).  
63 This Allee effect creates a strong coupling between beetle host selection behavior and host tree susceptibility  
64 to attack (Raffa and Berryman 1983, Logan et al. 1998). Under normal conditions, weakened trees are  
65 the most susceptible to attack and will be the main targets of aggressive bark beetles like the western pine  
66 beetle (Bentz et al. 2010, Raffa et al. 2015). A key defense mechanism of trees to bark beetle attack is to  
67 flood beetle bore holes with resin, which physically expels beetles and may interrupt beetle communication  
68 (Raffa et al. 2015). Under severe water stress, trees no longer have the resources available to mount this  
69 defense (Kolb et al. 2016) and thus prolonged drought can often trigger increased bark beetle-induced tree  
70 mortality as average tree vigor declines (Bentz et al. 2010). As local beetle density increases due to successful  
71 reproduction on spatially-aggregated weakened trees, as might occur in a prolonged drought, mass attacks  
72 become capable of overwhelming any tree’s defenses and even healthy trees become susceptible (Bentz et  
73 al. 2010, Raffa et al. 2015). Thus, water stress can be a key determinant of whether individual trees are  
74 susceptible to bark beetle attack under many conditions, and this environmental condition may interact with  
75 other forest features, such as tree size, to drive susceptibility under extreme conditions (Bentz et al. 2010,  
76 Stephenson et al. 2019).

77 Forest structure— often characterized as the spatial distribution, size, and species composition of trees— also  
78 strongly influences western pine beetle activity. For instance, high-density forests are more prone to bark  
79 beetle attacks, and several mechanism likely underlie this phenomenon (Fettig 2012). A high-density forest  
80 may experience greater bark beetle-induced tree mortality for several reasons including: a) host availability is  
81 high and shorter dispersal distances facilitate successful colonization of those hosts (Miller and Keen 1960,  
82 Berryman 1982, Fettig et al. 2007); b) high host availability reduces the chance of individual beetles wasting  
83 their limited resources flying to and landing on a non-host tree (Moeck et al. 1981, Evenden et al. 2014); c)  
84 crowded trees experience greater competition for water resources and thus average tree resistance is lower  
85 (Hayes et al. 2009); or d) smaller gaps between trees protect pheromone plumes from dissipation by the wind  
86 and thus enhance intraspecific beetle communication (Thistle et al. 2004). Additionally, tree size affects bark  
87 beetle host selection behavior as smaller trees tend to have less capacity for resisting attack, but larger trees  
88 represent a more desirable target because their thicker phloem provides greater nutritional value (Chubaty et  
89 al. 2009, Graf et al. 2012). Tree density thus paints a fundamentally limited picture of the mechanism by  
90 which forest structure affects bark beetle disturbance, but *complex* forest structure— with explicit recognition  
91 of tree size, species composition (e.g., host versus non-host composition), and local tree density— should  
92 more appropriately capture the ecological processes underlying insect-induced tree mortality. Additionally,

93 considering the effects of complex forest structure simultaneously to the effects of environmental conditions  
94 may help refine our understanding of observed patterns of tree mortality in the recent California hot drought.

95 The vast spatial extent of tree mortality in the 2012 to 2015 California hot drought (USDAFS 2019) challenges  
96 our ability to simultaneously consider how broad-scale environmental conditions may interact with local,  
97 complex forest structure to affect the dynamic between bark beetle host selection and host tree susceptibility  
98 to attack (Anderegg et al. 2015, Stephenson et al. 2019). Measuring complex forest structure generally  
99 requires expensive instrumentation (Kane et al. 2014, Asner et al. 2016) or labor-intensive field surveys  
100 (Larson and Churchill 2012, Stephenson et al. 2019), which constrains survey extent and frequency. Small,  
101 unhumanned aerial systems (sUAS) enable relatively fast and cheap remote imaging over dozens of hectares of  
102 forest, which can be used to measure complex forest structure at the individual tree scale (Morris et al. 2017,  
103 Shiklomanov et al. 2019). Distributing such surveys across an environmental gradient is a viable approach to  
104 overcoming the data acquisition challenge inherent in investigating phenomena with both a strong local- and  
105 a strong broad-scale component.

106 We used ultra-high resolution, drone-derived remote sensing data over a network of 32 sites in Sierra Nevada  
107 yellow pine/mixed-conifer forests spanning 1000m of elevation and 350km of latitude and covering a total of  
108 9 square kilometers to ask how broad-scale environmental conditions interacted with local, complex forest  
109 structure to affect the probability of tree mortality during the cumulative tree mortality event of 2012 to  
110 2018. We asked:

- 111 1. How does host tree density and average host tree size affect the severity of western pine beetle  
112 disturbance?
- 113 2. How does tree density of all species (hereafter “overall density”) and average tree size of all species  
114 (hereafter “overall size”) affect the severity of western pine beetle disturbance?
- 115 3. How does environmentally-driven tree moisture stress affect the severity of western pine beetle distur-  
116 bance?
- 117 4. Do the effects of forest structure and environmental condition on western pine beetle disturbance  
118 interact?

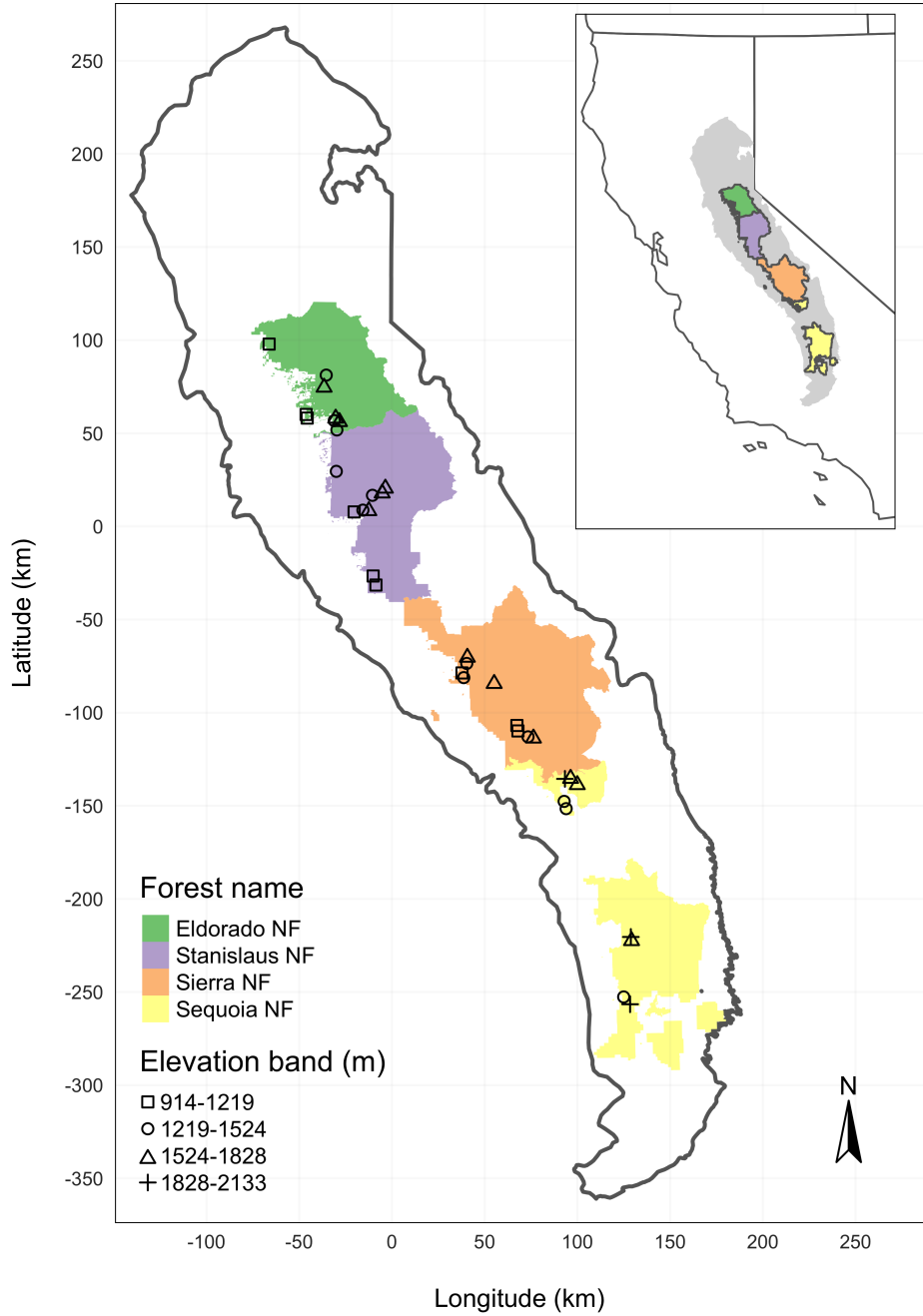


Figure 1: The network of field plots spanned a 350 km latitudinal gradient from the Eldorado National Forest in the north to the Sequoia National Forest in the south. Plots were stratified by three elevation bands in each forest, with the plots in the Sequoia National Forest (the southern-most National Forest) occupying elevation bands 305m above the three bands in the other National Forests in order to capture a similar community composition.

<sup>119</sup> **Methods**

<sup>120</sup> **Study system**

<sup>121</sup> The study sites were chosen to reflect typical west-side Sierra Nevada yellow pine/mixed-conifer forests and  
<sup>122</sup> were dominated by ponderosa pine trees, *Pinus ponderosa* (Fettig et al. 2019), whose primary bark beetle  
<sup>123</sup> predator in California is the western pine beetle (WPB), *Dendroctonus brevicomis*. The typical life cycle  
<sup>124</sup> of WPBs consists of pioneer beetles dispersing to a new host tree, determining the host's susceptibility to  
<sup>125</sup> attack, and using pheromone signals to attract other WPBs. The attracted WPBs mass attack the tree by  
<sup>126</sup> boring into its inner bark, laying eggs, and dying, leaving their offspring to develop inside the doomed tree  
<sup>127</sup> before themselves dispersing to a new potential host (Raffa et al. 2008). In California, the WPB can have 2-3  
<sup>128</sup> generations in a single year and can often out-compete its congener, the mountain pine beetle, *Dendroctonus*  
<sup>129</sup> *ponderosa* (MPB), for the ponderosa pine host (Fettig et al. 2019).

<sup>130</sup> We built our study on 180 vegetation/forest insect monitoring plots at 36 sites established between 2016  
<sup>131</sup> and 2017 by Fettig et al. (2019) (Figure 1). These established plots were located in WPB-attacked, yellow  
<sup>132</sup> pine/mixed-conifer forests across the Eldorado, Stanislaus, Sierra and Sequoia National Forests and were  
<sup>133</sup> stratified by elevation (914-1219 meters [3000-4000 feet], 1219-1524 meters [4000-5000 feet], 1524-1828 meters  
<sup>134</sup> [5000-6000 feet] above sea level). In the Sequoia National Forest, the southernmost National Forest in our  
<sup>135</sup> study, plots were stratified with the lowest elevation band between 1219 and 1524 meters (4000-5000 feet) and  
<sup>136</sup> extended to an upper elevation band of 1828-2133 meters (6000-7000 feet) to capture a more similar forest  
<sup>137</sup> community composition as at the more northern National Forests. The sites have variable forest structure  
<sup>138</sup> and plot locations were selected in areas with >40% ponderosa pine basal area and >10% ponderosa pine  
<sup>139</sup> mortality. At each site, five 0.04 ha circular plots were installed along transects with between 80 and 200m  
<sup>140</sup> between each plot. In the field, Fettig et al. (2019) mapped all stem locations relative to the center of each  
<sup>141</sup> plot using azimuth/distance measurements. Tree identity to species, tree height, and diameter at breast  
<sup>142</sup> height (DBH) were recorded if DBH was greater than 6.35cm. Year of mortality was estimated based on  
<sup>143</sup> needle color and retention, if it wasn't directly observed between site visits. A small section of bark was  
<sup>144</sup> removed from dead trees to confirm insect activity. During the spring and early summer of 2018, all field  
<sup>145</sup> plots were revisited to assess whether dead trees had fallen (Fettig et al. 2019).

<sup>146</sup> **Instrumentation**

<sup>147</sup> Imagery was captured using a DJI Zenmuse X3 RGB camera (DJI 2015a) and a Micasense RedEdge3 5-band  
<sup>148</sup> multispectral camera (Micasense 2015). We mounted both of these instruments simultaneously on a DJI  
<sup>149</sup> Matrice 100 aircraft (DJI 2015b) using the DJI 3-axis stabilized gimbal for the Zenmuse X3 camera and a

150 Micasense angled fixed mount for the RedEdge3 camera. The gimbal and the angled fixed mount ensured  
151 both instruments were nadir-facing during image capture. Just prior to or after image capture at each site,  
152 we calibrated the RedEdge3 camera by taking an image of a calibration panel on the ground in full sun with  
153 known reflectance values for each of the 5 narrow bands (Table 1).

Table 1: Reflectance sensitivity of the Micasense Rededge3 camera. The calibration panel value represents the reflectance of the calibration panel for the given wavelength.

Band number	Band name	Center wavelength	Band width	Wavelength range	Panel reflectance
1	blue (b)	475	20	465-485	0.64
2	green (g)	560	20	550-570	0.64
3	red (r)	668	10	663-673	0.64
4	near infrared (nir)	840	40	820-860	0.6
5	red edge (re)	717	10	712-722	0.63

#### 154 Flight protocol

155 Image capture was conducted as close to solar noon as possible to minimize shadow effects (varying primarily  
156 due to site accessibility; always within 4 hours, usually within 2 hours). Prior to the aerial survey, two strips  
157 of bright orange drop cloth (~100cm x 15cm) were positioned as an “X” over the permanent monuments  
158 marking the center of the 5 field plots from Fettig et al. (2019).

159 For each of the 36 sites (containing 5 plots each), we captured imagery over the surrounding ~40 hectares of  
160 forested area using north-south aerial transects. For three sites, we surveyed less surrounding area in order to  
161 maintain visual and radio communication with the aircraft during flight which can be obstructed by rolling  
162 terrain or non-centrally available takeoff locations.

163 We preprogrammed aerial transects using Map Pilot for DJI on iOS flight software (hereafter Map Pilot)  
164 (DronesMadeEasy 2018). Using the Map Pilot software, we included an altitude adjustment along each  
165 aerial transect using a 1-arc-second digital elevation model (Farr et al. 2007) such that the aircraft’s altitude  
166 remained approximately constant at 120 meters above ground level in order to maintain consistent ground  
167 sampling distance (centimeters on the ground per pixel) in the imagery. Ground sampling distance was  
168 approximately 5 cm/px for the Zenmuse X3 RGB camera and approximately 8 cm/px for the RedEdge3  
169 multispectral camera. For this analysis, we dropped 4 sites whose imagery was of insufficient quality to  
170 process.

171 Structure from motion (SfM) processing requires highly overlapping images, especially in densely vegetated  
172 areas (Frey et al. 2018). We planned transects with 90% forward overlap and 90% side overlap at 100 meters  
173 below the lens. Thus, with flights being at 120 meters above ground level, we achieved slightly higher than  
174 90/90% overlap for objects under 20 meters tall (91.6/91.6% overlap at the ground). Overlap values were  
175 based on focal length (3.6mm), sensor width (6.2mm), and image dimension (4000x3000 pixels) parameters  
176 of the Zenmuse X3 camera. Images were captured at a constant rate of 1 image every 2 seconds for both  
177 cameras. A forward overlap of 90% at 100 meters translates to a flight speed of approximately 6.45 m/s and  
178 a side overlap of 90% at 100 meters translates to transects approximately 17.2 meters apart. The RedEdge3  
179 camera has a different focal length (5.4mm), sensor width (4.8mm), and image dimension (1280x960 pixels),  
180 which translates to image overlap of 80.7/80.7 % at 100m below the lens and 83.9/83.9 % at ground level.  
181 Approximately 1900 photos were captured over each 40 hectare survey area for each camera.

## 182 **Structure from Motion (SfM) processing**

183 We used structure from motion (SfM) to generate dense point clouds (Figure 2), digital surface models  
184 (Figure 3), and orthorectified reflectance maps (Figure 4) for each field site (Frey et al. 2018). We used  
185 Pix4Dmapper Cloud to process imagery using parameters ideal for images of a densely vegetated area taken  
186 by a multispectral camera. For 29 sites, we processed the RedEdge3 multispectral imagery alone. For three  
187 sites, we processed the RGB and the multispectral imagery in the same project to enhance the point density  
188 of the resulting point cloud. All SfM projects resulted in a single processing “block,” indicating that all  
189 images in the project were optimized and processed together.

## 190 **Creating canopy height models**

191 We classified each survey area’s dense point cloud into “ground” and “non-ground” points using a cloth  
192 simulation filter algorithm (Zhang et al. 2016) implemented in the `lidR` (Roussel et al. 2019) package. We  
193 rasterized the ground points using the `raster` package (Hijmans et al. 2019) to create a digital terrain model  
194 (Figure 5) representing the ground underneath the vegetation at 1 meter resolution. We created a canopy  
195 height model (Figure 6) by subtracting the digital terrain model from the digital surface model created in  
196 Pix4Dmapper.

## 197 **Tree detection**

198 We tested a total of 7 automatic tree detection algorithms and a total of 177 parameter sets on the canopy  
199 height model or the dense point cloud to locate trees within each site (Table 2). We used 3 parameter sets of  
200 a variable window filter using the `vwf()` function in the `ForestTools` (Plowright 2018) R package, including

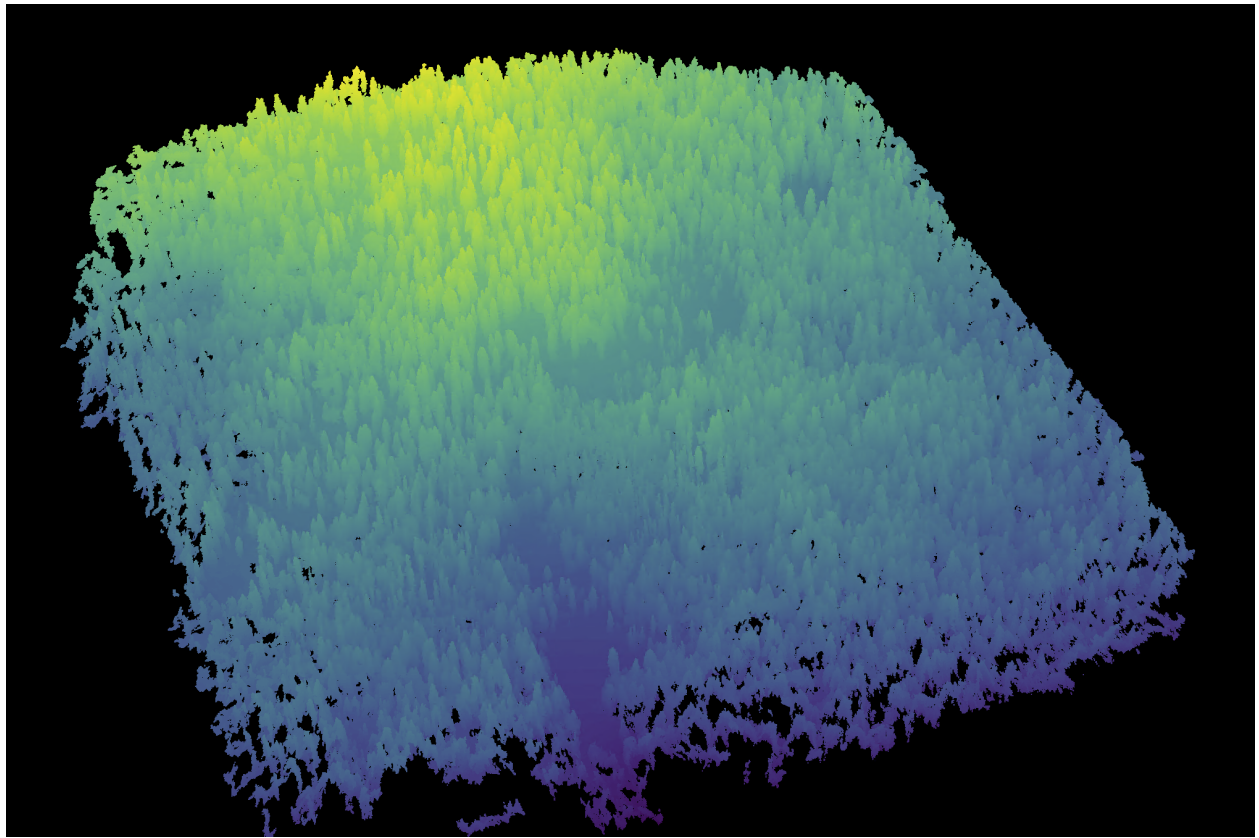


Figure 2: A dense point cloud representing ~40 hectares of forest is generated using Structure from Motion (SfM) processing of ~1900 images. The dense point cloud z- position represents the ground elevation plus the vegetation height.

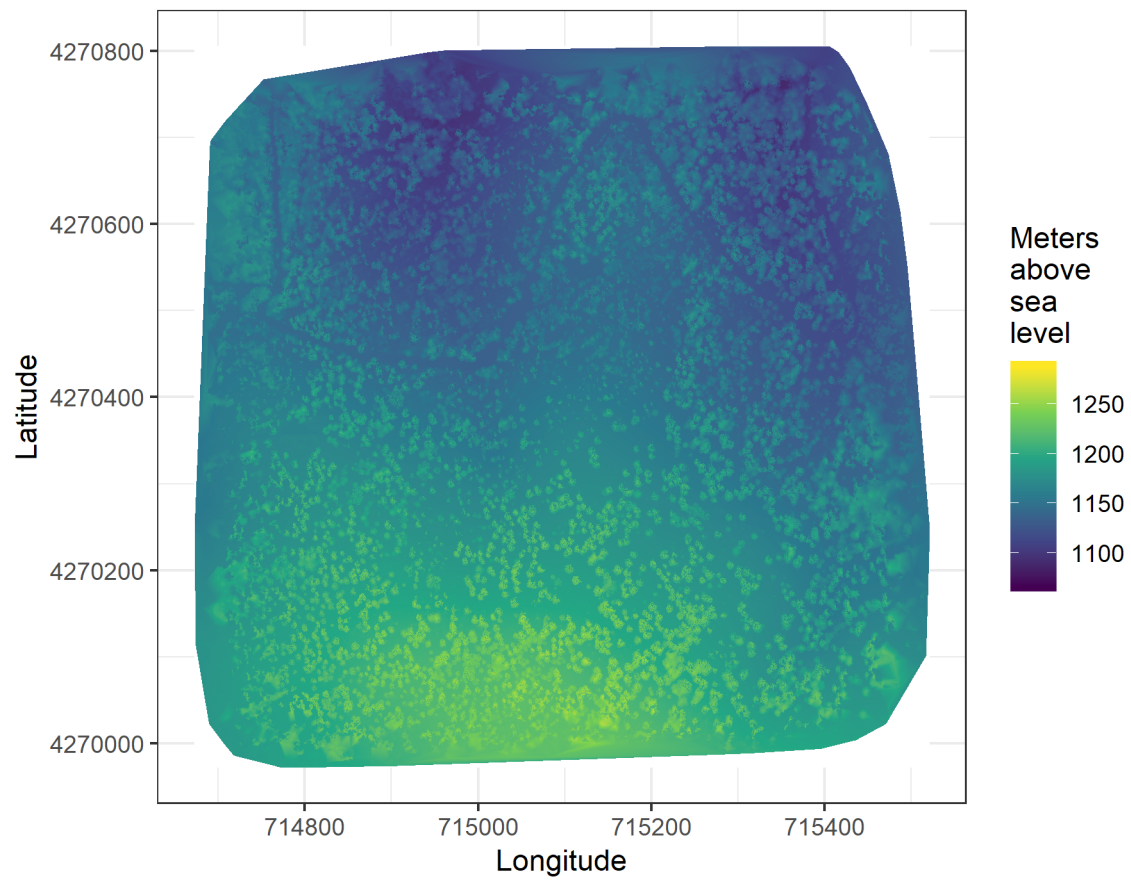


Figure 3: The digital surface model (DSM) is a 2-dimensional representation of the dense point cloud generated using structure from motion (SfM) processing. The DSM represents the ground elevation plus the vegetation height.

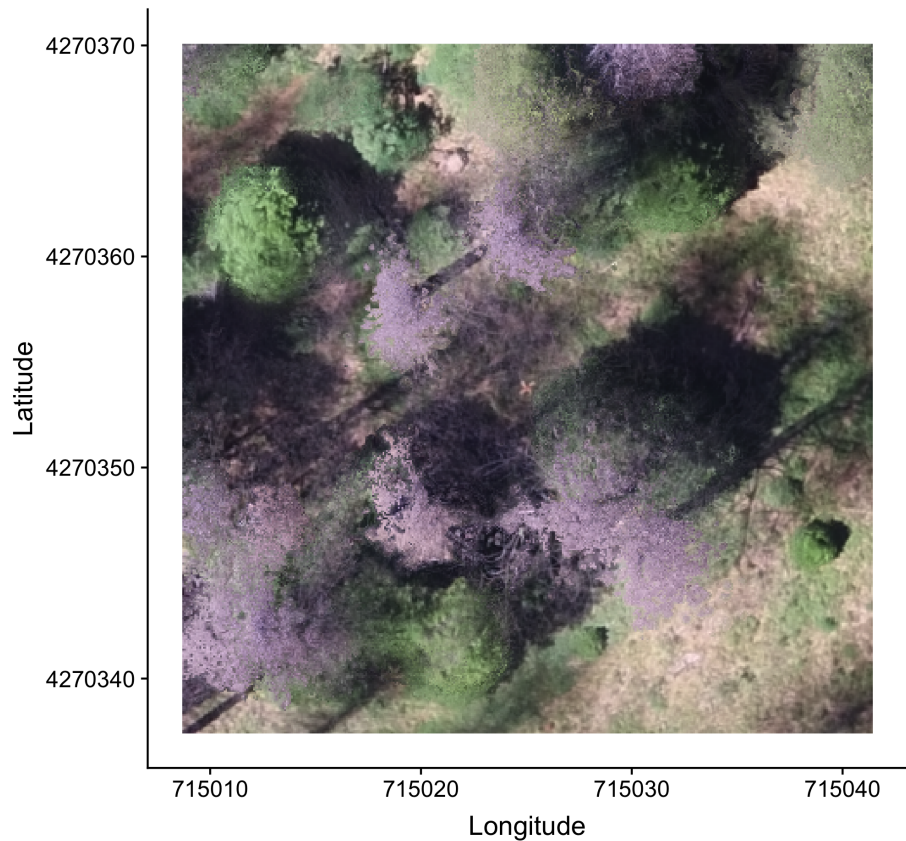


Figure 4: The orthomosaic for each of the 32 sites is generated with the Structure from Motion (SfM) processing, showing a top-down view of the whole survey area such that distances between objects in the scene are preserved and can be measured. Depicted is an example orthomosaic for one of the 32 sites cropped to the extent of a single ground plot (5 ground plots per site) showing the orange X placed at exactly the plot center prior to flight. The original orthomosaic for the whole site represents an area approximately 1000 times as large as the area depicted here.

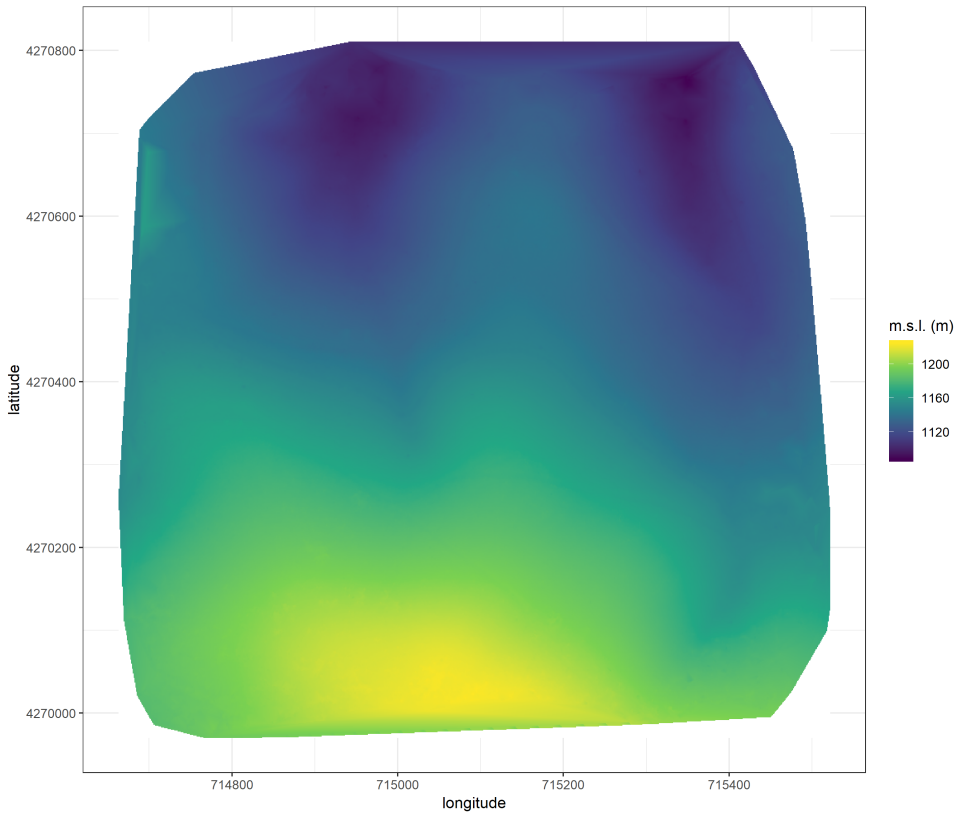


Figure 5: The digital terrain model (DTM) is generated by processing the dense point cloud using the cloth simulation filter algorithm (Zhang et al. 2016), which classifies points as ‘ground’ or ‘not-ground’ and then interpolates the ‘ground’ elevation using Delaunay triangulation for the rest of the dense point cloud footprint. The DTM represents the ground elevation without any vegetation.

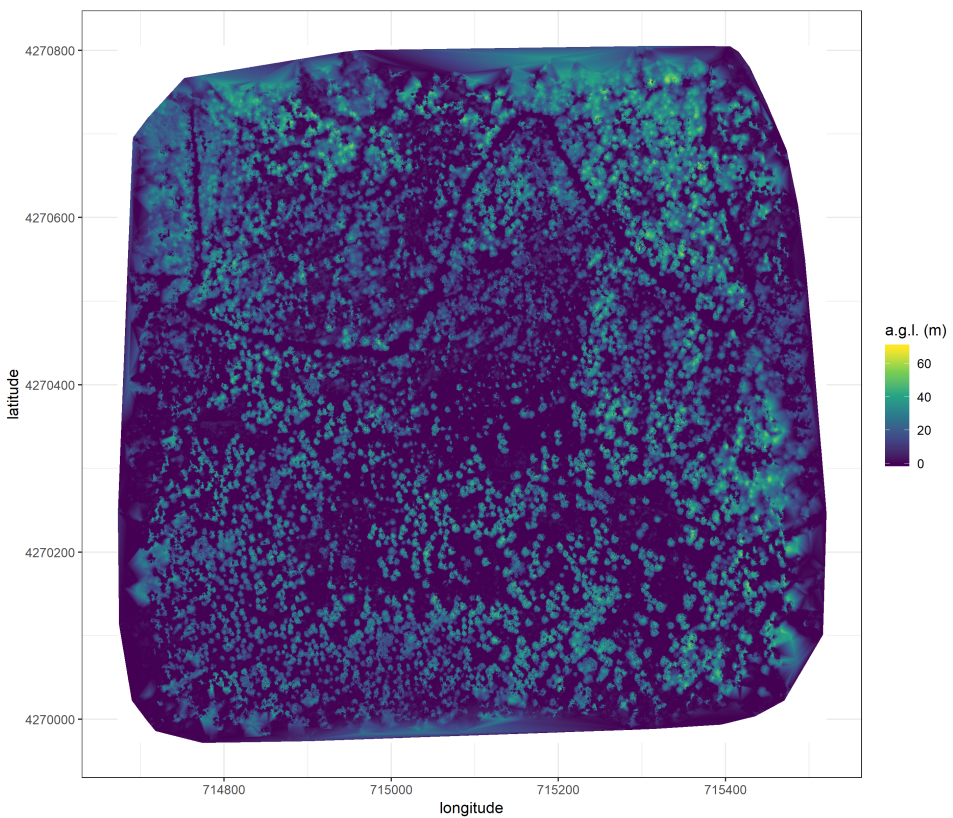


Figure 6: The canopy height model (CHM) is generated by subtracting the digital terrain model from the digital surface model. The CHM represents the height of all of the elevation above ground level.

201 the default `winFun` parameter for the `vwf()` function as well as the “pines” and “combined” functions from  
 202 Popescu and Wynne (2004) as the `winFun` parameter. We used 6 parameter sets of a local maximum filter  
 203 implemented in `lidR`. We used 131 parameter sets of the algorithm from Li et al. (2012), which operates on  
 204 the original point cloud. These parameter sets included those from Shin et al. (2018) and Jakubowski et  
 205 al. (2013). We used 3 parameter sets of the `watershed` algorithm implemented in `lidR`, which is a wrapper  
 206 for a function in the `EBImage` package (Pau et al. 2010). We used 3 parameter sets of `ptrees` (Vega et al.  
 207 2014) implemented in `lidR` (Roussel et al. 2019) and `lidRplugins` (Roussel 2019) and which operates on  
 208 the raw point cloud, without first normalizing it to height above ground level (i.e.. subtracting the ground  
 209 elevation from the dense point cloud). We used the default parameter set of the `multichm` (Eysn et al. 2015)  
 210 algorithm implemented in `lidR` (Roussel et al. 2019) and `lidRplugins` (Roussel 2019). Finally, we used 30  
 211 parameter sets of the experimental algorithm `lmfx` (Roussel 2019).

Table 2: Algorithm name, number of parameter sets tested for each algorithm, and references.

Algorithm	Parameter sets tested	Reference(s)
li2012	131	Li et al. (2012); Jakubowski et al. (2013); Shin et al. (2018)
lmfx	30	Roussel (2019)
localMaxima	6	Roussel et al. (2019)
multichm	1	Eysn et al. (2015)
ptrees	3	Vega et al. (2014)
vwf	3	Plowright (2018)
watershed	3	Pau et al. (2010)

## 212 Map ground data

213 Each orthorectified reflectance map was inspected to locate the 5 orange “X”s marking the center of the field  
 214 plots (Figure 4), though some plot centers were obscured due to dense interlocking tree crowns or because a  
 215 plot center was located directly under a single tree crown. We were able to locate 110 out of 180 field plots  
 216 and were then able to use these plots for validation of automated tree detection algorithms. We used the `sf`  
 217 package (Pebesma et al. 2019) to convert distance-from-center and azimuth measurements of each tree in the  
 218 ground plots to an x-y position on the SfM-derived reflectance map using the x-y position of the orange X  
 219 visible in the reflectance map as the center.

**220 Correspondence of automatic tree detection with ground data**

**221** We calculated 7 forest structure metrics for each field plot using the ground data collected by Fettig et al.  
**222** (2019): total number of trees, number of trees greater than 15 meters, mean height of trees, 25<sup>th</sup> percentile  
**223** tree height, 75<sup>th</sup> percentile tree height, mean distance to nearest tree neighbor, mean distance to 2<sup>nd</sup> nearest  
**224** neighbor.

**225** For each tree detection algorithm and parameter set described above, we calculated the same set of 7 structure  
**226** metrics within the footprint of the validation field plots. We calculated the Pearson's correlation and root  
**227** mean square error (RMSE) between the ground data and the aerial data for each of the 7 structure metrics  
**228** for each of the 177 automatic tree detection algorithms/parameter sets.

**229** For each algorithm and parameter set, we calculated its performance relative to other algorithms as whether  
**230** its Pearson's correlation was within 5% of the highest Pearson's correlation as well as whether its RMSE  
**231** was within 5% of the lowest RMSE. For each algorithm/parameter set, we summed the number of forest  
**232** structure metrics for which it reached these 5% thresholds. For automatically detecting trees across the whole  
**233** study, we selected the algorithm/parameter set that performed well across the most number of forest metrics  
**234** (Figure 7).

**235 Segmentation of crowns**

**236** We delineated individual tree crowns with a marker controlled watershed segmentation algorithm (Meyer and  
**237** Beucher 1990) using the detected treetops as markers implemented in the **ForestTools** package (Plowright  
**238** 2018). If the automatic segmentation algorithm failed to generate a crown segment for a detected tree (e.g.,  
**239** often snags with a very small crown footprint), a circular crown was generated with a radius of 0.5 meters. If  
**240** the segmentation generated multiple polygons for a single detected tree, only the polygon containing the  
**241** detected tree was retained (Figure 8). Image overlap decreases near the edges of the overall flight path, which  
**242** reduces the quality of the SfM processing in those areas. Thus, we excluded segmented crowns within 35  
**243** meters of the edge of the survey area. Given the narrower field of view of the RedEdge3 multispectral camera  
**244** versus the X3 RGB camera whose optical parameters were used to define the ~40 hectare survey area around  
**245** each site, as well as the 35 meter additional buffering, the survey area at each site was approximately 30  
**246** hectares (Table 3).

**247** We used the **velox** package (Hunziker 2017) to extract all the pixel values from the orthorectified reflectance  
**248** map for each of the 5 narrow bands within each segmented crown polygon. Per pixel, we additionally  
**249** calculated the normalized difference vegetation index (NDVI; Rouse et al. (1973)), the normalized difference

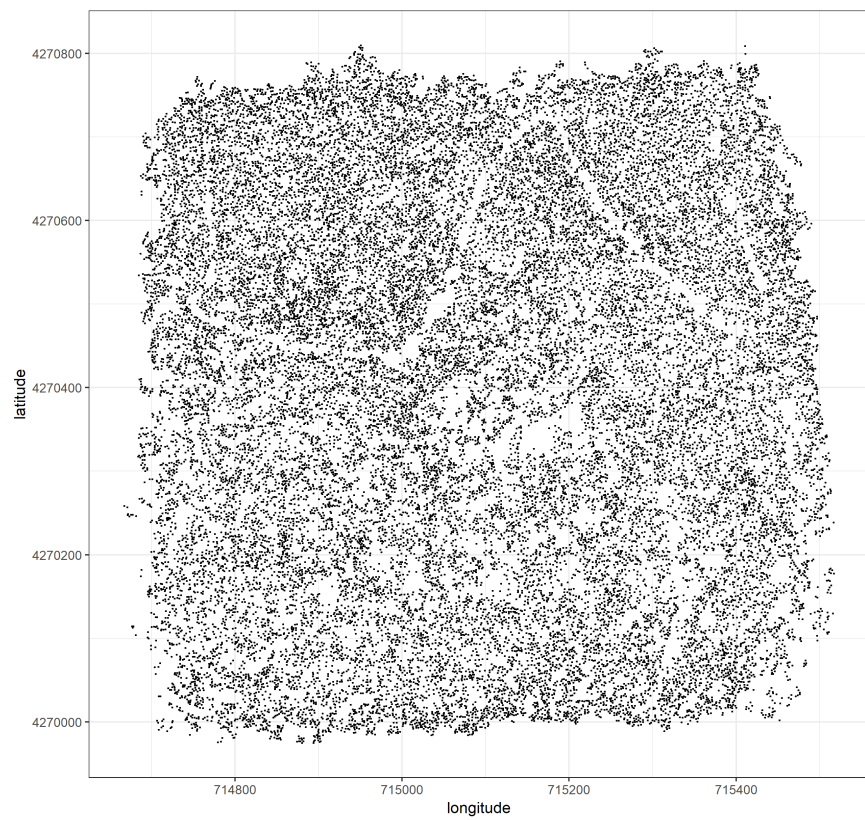


Figure 7: Tree locations are detected using the `lmfx` (Roussel et al. 2019) treetop detection algorithm on the dense point cloud.

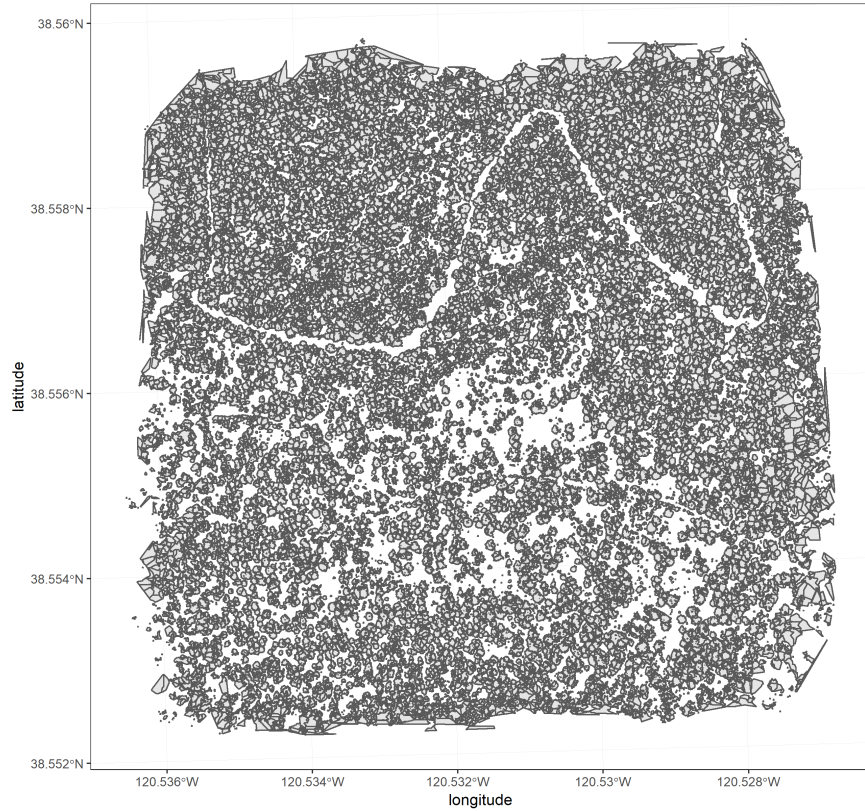


Figure 8: Individual crowns are delineated using a marker controlled watershed segmentation algorithm (Meyer and Beucher 1990, Plowright 2018) on the canopy height model (CHM) using the detected tree locations as a priority map. If the algorithm failed to delineate a crown for a tree that was identified in the tree detection step, a circular crown with a 0.5m buffer centered on point location of the detected tree was added as a crown.

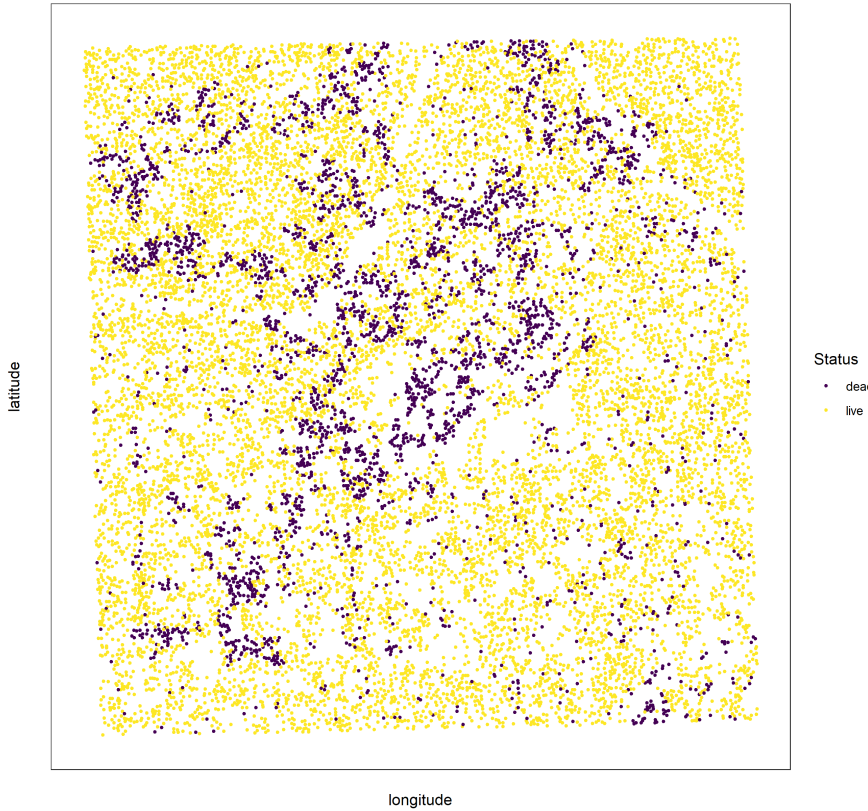


Figure 9: Each tree is classified as live or dead by extracting the pixel values from the 5 narrow bands of the Rededge3 camera (and 5 derived bands— see methods) in the orthomosaic within each segmented tree crown of the detected trees, taking their mean value, and using those means to predict live/dead status with a boosted logistic regression previously trained on a hand-classified set of segmented crowns from across the study area.

250 red edge (NDRE; Gitelson and Merzlyak (1994)), the red-green index (RGI; Coops et al. (2006)), the red  
 251 edge chlorophyll index ( $CI_{red\ edge}$ ; Clevers and Gitelson (2013)), and the green chlorophyll index ( $CI_{green}$ ;  
 252 Clevers and Gitelson (2013)). For each crown polygon, we calculated the mean value for each raw and derived  
 253 reflectance band (5 raw; 5 derived).

#### 254 Classification of trees

255 We overlaid the segmented crowns on the reflectance maps from 20 sites spanning the latitudinal and elevation  
 256 gradient in the study. Using QGIS, we hand classified 564 trees as live/dead (Figure 9) and as one of 5  
 257 dominant species in the study area (*Pinus ponderosa*, *Pinus lambertiana*, *Abies concolor*, *Calocedrus decurrens*,  
 258 or *Quercus kelloggii*) using the mapped ground data as a guide. We treated all trees classified as ponderosa  
 259 pine as a “host” tree and all other species as “non-host” trees (Figure 10).

260 We used all 10 mean values of the reflectance bands for each tree crown polygon to predict whether the hand

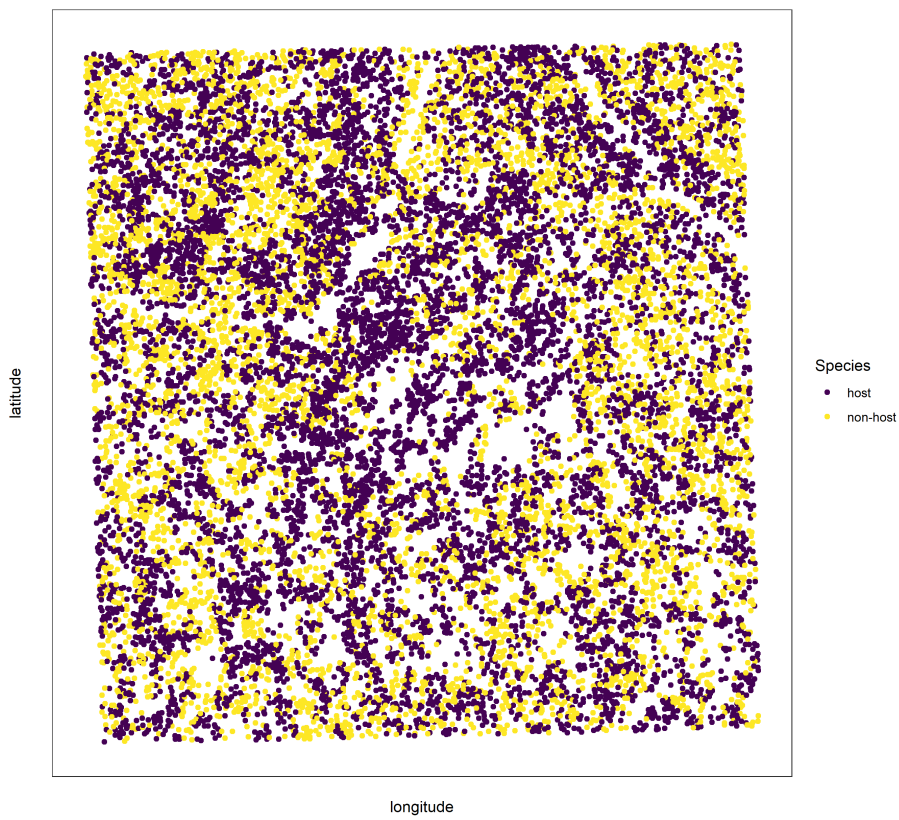


Figure 10: For each live tree, we classified its species using the same means of extracted pixel values across the 5 Rededge3 narrow bands (and 5 derived bands) as predictors in a regularized discriminant analysis previously trained on a hand-classified set of segmented crowns from across the study area.

261 classified trees were alive or dead using a boosted logistic regression model implemented in the **caret** package  
262 (accuracy of live/dead classification on a withheld test dataset: 97.3%) (Kuhn 2008). For just the living trees,  
263 we similarly used all 10 reflectance values to predict the tree species using regularized discriminant analysis  
264 implemented in the **caret** package (accuracy of species classification on a withheld testing dataset: 66.7%;  
265 accuracy of WPB host/non-WPB-host (i.e., ponderosa pine versus other tree species) on a withheld testing  
266 dataset: 74.4%).

267 Finally, we used these models to classify all tree crowns in the data set as alive or dead as well as the species  
268 of living trees.

#### 269 **Allometric scaling of height to quadratic mean diameter**

270 We converted the height of each tree determined using the canopy height model to its diameter at breast  
271 height, 1.37m (DBH). Using the tree height and DBH ground data from Fettig et al. (2019), we fit a simple  
272 linear regression to predict DBH from height for each of the 5 dominant species. Using the model-classified  
273 tree species of each segmented tree, we used the corresponding linear relationship for that species to estimate  
274 the DBH given the tree's height. We then calculated the quadratic mean diameter for each 20m x 20m cell as  
275 the square root of the average squared diameter of trees within the cell.

#### 276 **Note on assumptions about dead trees**

277 For the purposes of this study, we assumed that all dead trees were ponderosa pine and were thus host trees  
278 for the western pine beetle. This is a reasonably good assumption for our study area, given that Fettig et al.  
279 (2019) found that 73.4% of the dead trees in the coincident ground plots were ponderosa pine. The species  
280 contributing to the next highest proportion of dead trees was incense cedar which represented 18.72% of the  
281 dead trees in the ground plots. Incense cedar is not a potential host of the western pine beetle, and different  
282 forest structure/environment conditions can dictate the dynamic between forest insects and their host tree  
283 species (Stephenson et al. 2019). While the detected mortality is most likely to be ponderosa pine, it is  
284 critical to interpret our results with this known limitation in mind.

#### 285 **Rasterizing individual tree data**

286 Because the tree detection algorithms were validated against ground data at the plot level, we rasterized the  
287 classified trees at a spatial resolution similar to that of the ground plots (Figure 11). That is, we rasterized  
288 the individual tree data to 20m x 20m pixels equaling 400 m<sup>2</sup>, and the circular ground plots with 11.35m  
289 radius covered 404 m<sup>2</sup>. In each raster cell, we calculated the: number of live trees, number of dead trees,

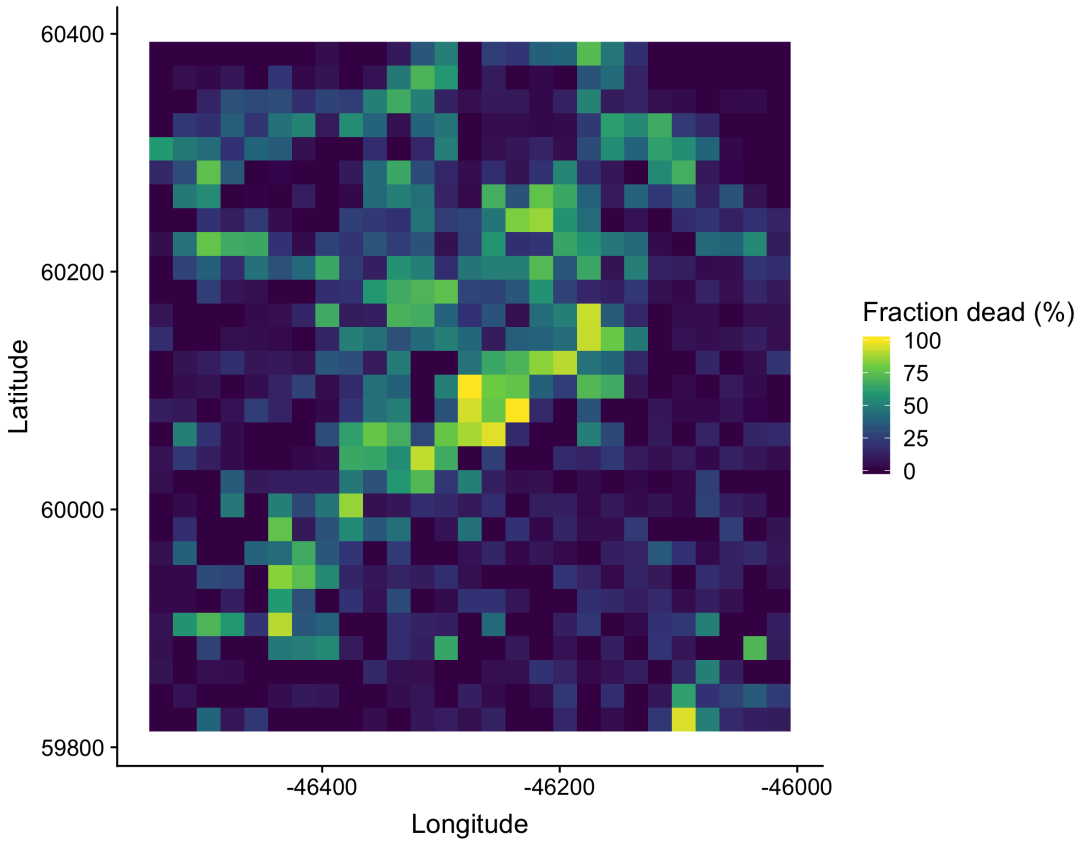


Figure 11: We rasterized the individual tree data by aggregating values to 20m x 20m cells. This example shows the proportion of dead trees per cell for the same example site as in the previous figures.

290 number of ponderosa pine trees, total number of trees (of all species, including ponderosa pine), quadratic  
291 mean diameter (QMD) of ponderosa pine trees, and QMD of all trees of any species (overall QMD). We  
292 converted the count of ponderosa pine trees and the total tree count to a density measurement of trees per  
293 hectare (tpha) by multiplying the counts in each 20m x 20m cell by 25 to create a “host density” and an  
294 “overall density” variable per cell.

## 295 **Environmental data**

296 We used climatic water deficit (CWD) (Stephenson 1998) from the 1981-2010 mean value of the basin  
297 characterization model (Flint et al. 2013) as an integrated measure of temperature and moisture conditions  
298 for each of the 32 sites. Higher values of CWD correspond to hotter, drier conditions and lower values  
299 correspond to cooler, wetter conditions. CWD has been shown to correlate well with broad patterns of tree  
300 mortality in the Sierra Nevada (Young et al. 2017) as well as bark beetle-induced tree mortality (Millar et al.  
301 2012). We converted the CWD value for each site into a z-score representing that site’s deviation from the  
302 mean CWD across the climatic range of Sierra Nevada ponderosa pine as determined from 179 herbarium  
303 records described in Baldwin et al. (2017). Thus, a CWD z-score of one would indicate that the CWD at  
304 that site is one standard deviation hotter/drier than the mean CWD across all geolocated herbarium records  
305 for ponderosa pine in the Sierra Nevada.

## 306 **Statistical model**

307 We used a generalized linear model with a zero-inflated binomial response and a logit link to predict the  
308 probability of ponderosa pine mortality within each 20m x 20m cell as a function of the crossed effects of  
309 ponderosa pine quadratic mean diameter and density added to the crossed effect of quadratic mean diameter  
310 and density of trees of all species in each cell (hereafter “overall quadratic mean diameter” and “overall  
311 density”), as well as the interaction of each summand with climatic water deficit at each site.

312 To measure and account for spatial autocorrelation of the bark beetle behavioral processes underlying  
313 ponderosa pine mortality, we subsampled the data at each site to a random selection of 200, 20m x 20m cells  
314 representing approximately 27.5% of the surveyed area. With these subsampled data, we included a separate  
315 exact Gaussian process term per site of the interaction between the x- and y-position of each cell using the  
316 `gp()` function in the `brms` package (Bürkner 2017). The Gaussian process estimates the spatial covariance in  
317 the response variable (log-odds of ponderosa pine mortality) jointly with the effects of the other covariates.

$$y_{i,j} \sim \begin{cases} 0, & p \\ Binom(n_i, \pi_i), & 1 - p \end{cases}$$

$\text{logit}(\pi_i) = \beta_0 +$

$$\beta_1 X_{cwd,j} +$$

$$\beta_1 X_{cwd,j} (\beta_2 X_{\text{pip}oQMD,i} + \beta_3 X_{\text{pip}o\text{Density},i} + \beta_4 X_{\text{pip}oQMD,i} X_{\text{pip}o\text{Density},i}) +$$

$$\beta_1 X_{cwd,j} (\beta_5 X_{\text{overall}QMD,i} + \beta_6 X_{\text{overall}\text{Density},i} + \beta_7 X_{\text{overall}QMD,i} X_{\text{overall}\text{Density},i}) +$$

$$\mathcal{GP}_j(x_i, y_i)$$

318 Where  $y_i$  is the number of dead trees in cell  $i$ ,  $n_i$  is the sum of the dead trees (assumed to be ponderosa pine)  
 319 and live ponderosa pine trees in cell  $i$ ,  $\pi_i$  is the probability of ponderosa pine tree mortality in cell  $i$ ,  $p$  is the  
 320 probability of there being zero dead trees in a cell arising as a result of an unmodeled process,  $X_{cwd,j}$  is the  
 321 z-score of climatic water deficit for site  $j$ ,  $X_{\text{pip}oQMD,i}$  is the scaled quadratic mean diameter of ponderosa  
 322 pine in cell  $i$ ,  $X_{\text{pip}o\text{Density},i}$  is the scaled density of ponderosa pine trees in cell  $i$ ,  $X_{\text{overall}QMD,i}$  is the scaled  
 323 quadratic mean diameter of all trees in cell  $i$ ,  $X_{\text{overall}\text{Density},i}$  is the scaled density of all trees in cell  $i$ ,  $x_i$   
 324 and  $y_i$  are the x- and y- coordinates of the centroid of the cell in an EPSG3310 coordinate reference system,  
 325 and  $\mathcal{GP}_j$  represents the exact Gaussian process describing the spatial covariance between cells at site  $j$ .  
 326 We used 4 chains with 2000 iterations each (1000 warmup, 1000 samples), and confirmed chain convergence  
 327 by ensuring all `Rhat` values were less than 1.1 (Brooks and Gelman 1998). We used posterior predictive  
 328 checks to visually confirm model performance by overlaying the density curves of the predicted number of  
 329 dead trees per cell over the observed number (Gabry et al. 2019). For the posterior predictive checks, we  
 330 used 50 random samples from the model fit to generate 50 density curves and ensured curves were centered  
 331 on the observed distribution, paying special attention to model performance at capturing counts of zero.

332 **Software and data availability**

333 All data are available via the Open Science Framework. Statistical analyses were performed using the `brms`  
 334 packages. With the exception of the SfM software (Pix4Dmapper Cloud) and the GIS software QGIS, all  
 335 data carpentry and analyses were performed using R (R Core Team 2018).

336 **Results**

Table 3: Site characteristics for each of the 32 sites. The site name consists of the forest name, elevation band, and rep separated by an underscore. The Eldorado National Forest is ‘eldo’, the Stanislaus National Forest is ‘stan’, the Sierra National Forest is ‘sier’, and the Sequoia National Forest is ‘sequ’. The elevation band represents the lower bounds of the 305 meter (1000 foot) elevation bands in feet. Thus ‘3k’ implies that site was located between 3,000 and 4,000 feet (914-1219 meters). Aerially detected mortality and density of the whole site is presented along with the mortality and density calculated from the ground data (aerial / ground). The density is measured in trees per hectare (tpha).

Site	CWD (mm)	CWD (z-score)	Survey area (ha)	% tree mortality (aerial/ground)	Density (tpha; aerial/ground)
eldo_3k_1	678	0.319	31.02	11/61	630/410
eldo_3k_2	706	0.501	30.61	12/36	444/647
eldo_3k_3	655	0.163	30.95	22/36	493/410
eldo_4k_1	570	-0.383	28.04	9/39	633/588
eldo_4k_2	642	0.0831	28.41	15/78	338/272
eldo_5k_1	663	0.219	28.44	11/44	662/544
eldo_5k_2	627	-0.0132	30.02	12/36	585/969
eldo_5k_3	599	-0.2	29.73	7/32	489/623
stan_3k_1	638	0.059	31.04	10/52	739/1038
stan_3k_2	739	0.713	18.78	40/78	434/405
stan_3k_3	762	0.859	30.1	22/41	558/326
stan_4k_1	540	-0.58	29.62	29/63	508/712
stan_4k_2	528	-0.658	30.54	18/56	482/257
stan_5k_1	524	-0.688	30.94	19/54	389/336
stan_5k_2	524	-0.685	29.94	21/44	399/623
sier_3k_1	764	0.871	30.42	19/48	651/850
sier_3k_2	768	0.898	30.05	20/77	439/153
sier_3k_3	773	0.932	29.77	32/77	511/460
sier_4k_1	841	1.38	30.43	54/51	576/539
sier_4k_2	764	0.877	29.3	33/57	499/855
sier_4k_3	688	0.383	26.39	48/59	454/499
sier_5k_1	722	0.599	14.59	41/43	631/717
sier_5k_2	710	0.523	27.53	53/74	477/455
sier_5k_3	779	0.968	28.93	33/43	569/484
sequ_4k_1	767	0.891	29.59	50/56	366/608

Site	CWD (mm)	CWD (z-score)	Survey area (ha)	% tree mortality (aerial/ground)	Density (tpha; aerial/ground)
sequ_4k_3	816	1.21	29.69	35/71	433/306
sequ_5k_1	718	0.577	27.12	35/52	364/445
sequ_5k_2	587	-0.274	29.1	45/43	478/499
sequ_5k_3	611	-0.117	31.34	42/48	349/494
sequ_6k_1	731	0.657	27.78	30/70	433/361
sequ_6k_2	690	0.39	11.83	26/43	699/934
sequ_6k_3	603	-0.174	26.51	36/32	536/692

337 **Tree detection**

338 We found that the experimental `lmfx` algorithm with parameter values of `dist2d = 1` and `ws = 2.5` (Roussel  
 339 et al. 2019) performed the best across 7 measures of forest structure as measured by Pearson’s correlation  
 340 with ground data (Table 4).

Table 4: Correlation and differences between the best performing tree detection algorithm (`lmfx` with `dist2d = 1` and `ws = 2.5`) and the ground data. An asterisk next to the correlation or RMSE indicates that this value was within 5% of the value of the best-performing algorithm/parameter set. Ground mean represents the mean value of the forest metric across the 110 ground plots that were visible from the sUAS-derived imagery. The median error is calculated as the median of the differences between the air and ground values for the 110 visible plots. Thus, a positive number indicates an overestimate by the sUAS workflow and a negative number indicates an underestimate.

Forest structure metric	Ground mean	Correlation with ground	RMSE	Median error
total tree count	19	0.67*	8.68*	2
count of trees > 15m	9.9	0.43	7.38	0
distance to 1st neighbor (m)	2.8	0.55*	1.16*	0.26
distance to 2nd neighbor (m)	4.3	0.61*	1.70*	0.12
height (m); 25th percentile	12	0.16	8.46	-1.2
height (m); mean	18	0.29	7.81*	-2.3
height (m); 75th percentile	25	0.35	10.33*	-4

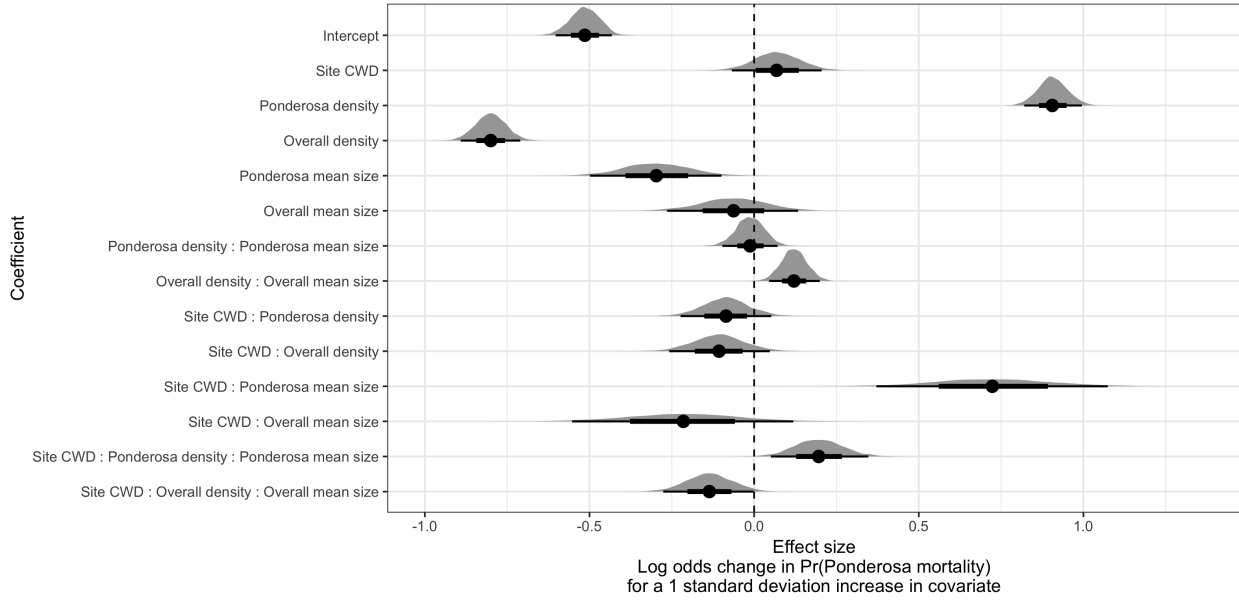


Figure 12: Posterior distributions of effect size from zero-inflated binomial model predicting the probability of ponderosa pine mortality in a 20m x 20m cell given forest structure characteristics of host trees and all trees within the cell, as well as a site-level climatic water deficit. The gray density distribution for each model covariate represents the density of the posterior distribution, the point underneath each density curve represents the median of the estimate, the bold interval surrounding the point estimate represents the 66% credible interval, and the thin interval surrounding the point estimate represents the 95% credible interval.

#### **341    Effect of local structure and regional climate on western pine beetle severity**

**342** We detected a small, generally positive main effect of climatic water deficit on the probability of ponderosa  
**343** pine mortality within each 20m x 20m cell (Figure 12).

**344** We found a strongly positive main effect of ponderosa pine local density, with greater density increasing the  
**345** probability of ponderosa pine mortality. Conversely, we found a strong negative effect of overall tree density  
**346** (i.e., including both ponderosa pine and non-host species) such that additional non-host trees in a 20m x 20m  
**347** cell (for the same number of host trees) would decrease the probability of ponderosa pine mortality (Figure  
**348** 12).

**349** We found a generally negative effect of quadratic mean diameter of ponderosa pine on the probability of  
**350** ponderosa mortality, suggesting that the western pine beetle attacked smaller trees, on average. There was a  
**351** strong positive interaction between the climatic water deficit and ponderosa pine quadratic mean diameter,  
**352** such that larger trees were more likely to increase the probability of ponderosa mortality in hotter, drier sites  
**353** (Figure 13).

**354** There was a positive interaction between overall tree density and overall quadratic mean diameter, such that  
**355** denser stands with larger trees did lead to greater ponderosa pine mortality, though the main effects of each

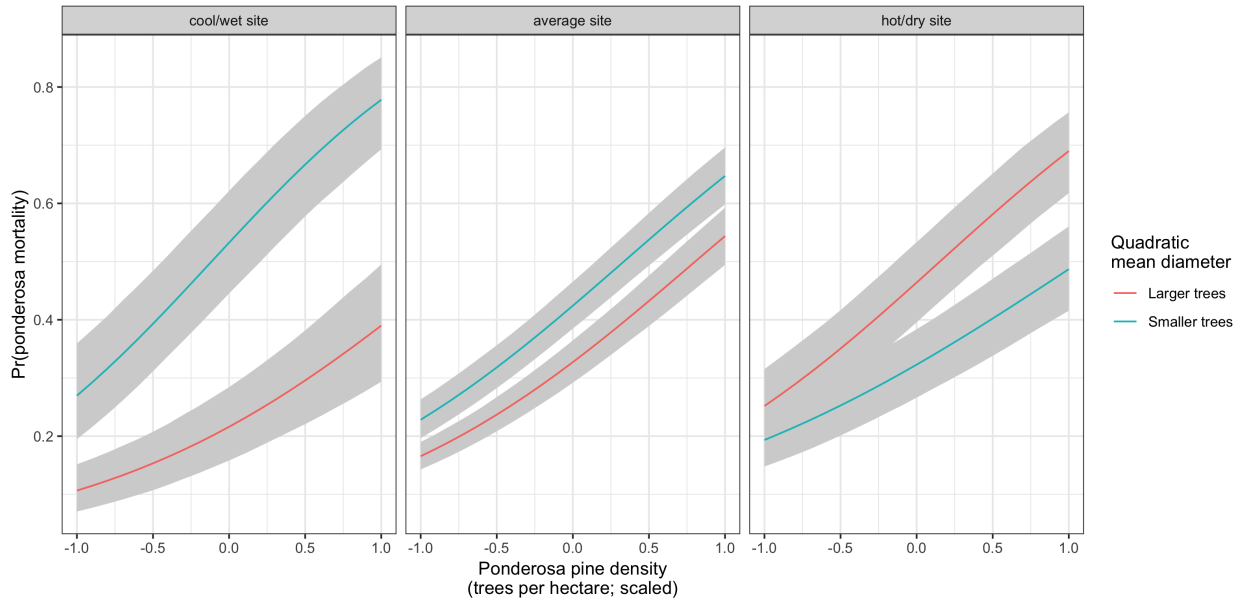


Figure 13: Line version of model results with 95% credible intervals showing primary influence of ponderosa pine structure on the probability of ponderosa pine mortality, and the interaction across climatic water deficit. The ‘larger trees’ line represents the quadratic mean diameter of ponderosa pine 0.7 standard deviations above the mean, and the ‘smaller trees’ line represents the quadratic mean diameter of ponderosa pine 0.7 standard deviations below the mean.

<sup>356</sup> of these variables were weakly negative (Figure 12).

## <sup>357</sup> Discussion

<sup>358</sup> We found that host tree density is a dominant driver of host mortality during elevated levels of bark beetle  
<sup>359</sup> activity, likely due to energy costs associated with beetles navigating forests with many non-hosts available.  
<sup>360</sup> We also found that, even within a single forest insect/tree species pairing, in the same extreme drought,  
<sup>361</sup> and conditional upon high levels of western pine beetle activity, host tree size may still strongly affect  
<sup>362</sup> insect-induced tree mortality in different ways depending on background environmental conditions of water  
<sup>363</sup> stress. We suggest that this may indicate different stages of bark beetle disturbance throughout the Sierra  
<sup>364</sup> yellow pine/mixed-conifer system, with “outbreak” thresholds surpassed at the hottest, driest sites where  
<sup>365</sup> larger trees led to more likely host mortality, but not yet surpassed in cooler, wetter sites, where smaller trees  
<sup>366</sup> led to more likely host mortality.

## <sup>367</sup> Broad-scale environmental condition

<sup>368</sup> We were surprised to only find a weakly positive main effect of climatic water deficit on the probability of  
<sup>369</sup> ponderosa mortality, though an effect did materialize through its interaction with forest structure. We did

370 not measure tree water stress at an individual tree level as in other recent work (Stephenson et al. 2019), and  
371 were instead treating climatic water deficit as a general indicator of tree stress following results of coarser-scale  
372 studies (Asner et al. 2016, Young et al. 2017) which may have contributed to our failure to detect a strong  
373 effect. Also, our entire study area experienced the same extreme hot drought between 2012 and 2015 and the  
374 variation of mortality explained by a main effect of climatic water deficit may be dampened when most trees  
375 are experiencing a high degree of water stress (Floyd et al. 2009, Fettig et al. 2019).

376 **Strength of support for different “density increases mortality” hypotheses**

377 The strongest effect on the probability of host mortality was the local host density within each 20m x 20m  
378 cell. Host availability has been shown to have a strong influence on the prevalence of host mortality (Raffa  
379 and Berryman 1987). This can arise as beetles require shorter flights to disperse to new hosts and beetles are  
380 less likely to land on a non-host tree which imposes a “sunk cost” of energy expenditure in getting to that  
381 tree. Reduced dispersal distances to host trees likely favors successful bark beetle attacks, but we calibrated  
382 our aerial tree detection to ~400 m<sup>2</sup> areas rather than to individual tree locations so don’t have the data  
383 precision to address this hypothesis directly. Because we also found a strong negative effect of overall tree  
384 density (host plus non-host) within each cell while accounting for host density, we suspect that the positive  
385 association between host density and host mortality might be driven by increasing the frequency that western  
386 pine beetles land on their preferred host and avoid expending energy flying to non-hosts. The negative  
387 relationship that we detected between overall tree density and host mortality corroborates findings from  
388 Fettig et al. (2019) and perhaps the “sunk cost” of landing on non-hosts explains those findings, though  
389 Fettig et al. (2019) didn’t simultaneously model the effect of host density. In general, Hayes et al. (2009)  
390 and Fettig et al. (2019) found that measures of host availability explained less variation in mortality than  
391 measures of overall tree density, but those conclusions were based on a response variable of “total number of  
392 dead host trees,” rather than the number of dead host trees conditional on the total number of host trees as  
393 in our study (i.e., a binomial response).

394 Counter to our expectations, we found an overall negative effect of host tree mean size on the probability of  
395 host mortality. Generally, smaller trees are easier for western pine beetles to overwhelm in a mass attack and  
396 are prime targets under normal levels of tree water stress. However, larger trees are more nutritious and  
397 are therefore ideal targets if local bark beetle density is high enough to successfully initiate mass attack as  
398 can occur when many trees are under severe water stress (Bentz et al. 2010). In the recent hot drought, we  
399 expected that most trees would be under severe water stress, setting the stage for increasing beetle density,  
400 successful mass attacks, and targeting of larger trees. Larger average tree size in this case would therefore

401 lead to greater ponderosa pine mortality, as was found in coincident ground plots (Fettig et al. 2019) and  
402 other studies (Stephenson et al. 2019, Pile et al. 2019). One possible explanation for our finding is that our  
403 observations represent the cumulative mortality of trees during a multi-year drought event and its aftermath.  
404 Lower host tree mean size led to a greater probability of host mortality earlier in the drought (Pile et al.  
405 2019) and that signal might have persisted even as mortality continued to accumulate driven by other factors.

406 We did find a clear host tree size effect in its interaction with the climatic water deficit. In hot, dry sites,  
407 larger average host size increased the probability of host mortality while smaller host sizes increased the  
408 probability of host mortality in cool, wet sites. This suggests that the same bark beetle species was cueing  
409 into different aspects of forest structure across the environmental gradient. This represents an intraspecific  
410 version of the results of Stephenson et al. (2019), who found that insect-induced tree mortality in the same  
411 region during the same hot drought were driven by different factors for different tree species. For instance,  
412 Stephenson et al. (2019) found that ponderosa pine mortality was largely driven by host selection behavior  
413 of forest insects, where larger more nutritious trees were specifically targeted regardless of whether they  
414 exhibited signs of stress. In contrast, Stephenson et al. (2019) found that white fir mortality occurred  
415 predominantly in the slower growing, smaller, stressed trees. In our study, we found that, even within a single  
416 pairing of forest insect species and its host, the host tree size affected host mortality differently depending on  
417 the site-level climatic water deficit.

418 For aggressive bark beetles, massive tree mortality as observed from the 2012-2015 drought and its aftermath  
419 does not necessarily distinguish “endemic” from “outbreak” phases of bark beetle disturbance, which is  
420 instead distinguished by the underlying driver of bark beetle host selection behavior (Logan et al. 1998).  
421 “Endemic” phases are distinguished by environmental determinism, when beetles select hosts based on whether  
422 they are weakened in some way, often by environmental conditions. “Outbreak” phases are distinguished  
423 by dynamic determinism, when population dynamics reign—when local beetle density is high enough that  
424 intraspecific pheromone communication dominates host selection, successful mass attacks are likely, and even  
425 large healthy trees can be killed (White and Powell 1997, Logan et al. 1998). Despite high local levels of  
426 tree mortality across our study area (Fettig et al. 2019), our results from surveying the broader context  
427 surrounding coincident ground plots reveals different effects of host tree size depending on the climatic water  
428 deficit, and perhaps different stages of bark beetle disturbance across the environmental gradient. This may  
429 help explain the especially high host mortality in high host density, low host size cells that we observed  
430 in cool/wet sites (Figure 13). The smaller trees would presumably be nutritionally sub-optimal, and thus  
431 unexpected targets if the western pine beetle were indeed in an “outbreak” phase at these sites and able to  
432 attack even large, healthy trees. While trees were likely water stressed across the whole study due to the

433 extreme drought, we expected generally less water stress in the cool/wet sites, and generally higher water  
434 stress in the hot/dry sites (Asner et al. 2016, Young et al. 2017). Thus, it is possible that the observed  
435 mortality patterns across the Sierra Nevada during the 2012-2015 hot drought arose as synergistic alignment  
436 of environmental conditions and complex forest structure enabled the western pine beetle to cross thresholds  
437 of “outbreak” behavior in the hottest, driest sites but such an alignment was not present in the cooler, wetter  
438 sites (Raffa et al. 2008).

#### 439 **Limitations and future directions**

440 We have demonstrated that drones can be effective means of collecting data at multiple, vastly different  
441 spatial scales to investigate a single, multi-scale phenomenon– from meters in between trees, to hundreds of  
442 meters of elevation, to hundreds of thousands of meters of latitude. However, some limitations remain but  
443 could perhaps be overcome with further refinements in the use of this tool for forest ecology. Most of these  
444 limitations arise from tree detection and classification uncertainty, and thus it was imperative to work with  
445 field data for calibration and uncertainty reporting.

446 The greatest limitation in our study arising from classification uncertainty is in the assumption that all dead  
447 trees were ponderosa pine. We estimate from coincident ground plots that this is true approximately 73.4%  
448 of the time. Because tree mortality response to forest insects is species-specific, even with sympatric tree  
449 species during the same hot drought (Stephenson et al. 2019), we cannot entirely rule out that some of the  
450 mortality responses to complex forest structure that we observed arose from these species-specific responses.  
451 The overall community composition across our study area was not very different (Fettig et al. 2019), so we  
452 remain confident that the patterns we observed were driven primarily by the dynamic between the western  
453 pine beetle and ponderosa pine.

454 Our ability to detect trees using the geometry of the dense point clouds derived with the SfM was also  
455 limited. The horizontal accuracy of the tree detection was better than the vertical accuracy, which may result  
456 from a more significant error contribution by the ground-based calculations of tree height compared to tree  
457 position relative to plot center (Table 4). Both the horizontal and vertical accuracy would likely improve  
458 with better SfM point clouds, which requires imagery with more overlap. Frey et al. (2018) recently found  
459 that 95% overlap was preferable for generating dense point clouds, and we only achieved 91.6% overlap with  
460 the X3 RGB camera and 83.9% overlap with the multispectral camera. While our live/dead classification was  
461 fairly accurate (97.3% on a withheld dataset), our species classifier would likely benefit from better crown  
462 segmentation because the pixel-level reflectance values within each crown are averaged to characterize the  
463 “spectral signature” of each tree. With better delineation of each tree crown, the mean value of pixels within

464 each tree crown will likely be more representative of that tree's spectral signature. Better crown segmentation  
465 would most readily be achieved through greater overlap in imagery. Finally, we anticipate that computer  
466 vision and deep learning will prove helpful in overcoming some of these detection and classification challenges  
467 (Gray et al. 2019).

## 468 **Conclusions**

469 Climate change adaptation strategies emphasize reducing tree densities to restore forest resilience (North et  
470 al. 2015, Young et al. 2017), but understanding the optimal complex forest structure that can enable dry  
471 western U.S. forests to persist through disturbances such as insect attack will be vital for predicting how  
472 California forests may respond to these interventions. We've shown that drones can be a valuable tool for  
473 investigating how this complexity in forest structure combines with environmental conditions to shape forest  
474 insect disturbance.

475 Our results support conclusions of other researchers that management interventions to reduce the severity of  
476 bark beetle disturbance will benefit from generally reducing tree density (Young et al. 2017). However, in  
477 addition, our study suggests that outcomes will depend on whether the disturbance dynamic has crossed  
478 endemic to outbreak feedback thresholds (Raffa et al. 2008), which may be predicted by recent advances in  
479 disturbance forecasting (Preisler et al. 2017).

## 480 **Acknowledgements**

481 We gratefully acknowledge funding from the U.S.D.A. Forest Service Western Wildlands Environmental  
482 Threat Assessment Center (WWETAC) as well as Connie Millar for comments and guidance during the  
483 development of this project.

## 484 **References**

- 485 Anderegg, W. R. L., J. A. Hicke, R. A. Fisher, C. D. Allen, J. Aukema, B. Bentz, S. Hood, J. W. Lichstein,  
486 A. K. Macalady, N. McDowell, Y. Pan, K. Raffa, A. Sala, J. D. Shaw, N. L. Stephenson, C. Tague, and  
487 M. Zeppel. 2015. Tree mortality from drought, insects, and their interactions in a changing climate. New  
488 Phytologist 208:674–683.
- 489 Asner, G. P., P. G. Brodrick, C. B. Anderson, N. Vaughn, D. E. Knapp, and R. E. Martin. 2016. Progressive  
490 forest canopy water loss during the 20122015 California drought. Proceedings of the National Academy of

- 491 Sciences 113:E249–E255.
- 492 Baldwin, B. G., A. H. Thornhill, W. A. Freyman, D. D. Ackerly, M. M. Kling, N. Morueta-Holme, and B. D.  
493 Mishler. 2017. Species richness and endemism in the native flora of California. American Journal of Botany  
494 104:487–501.
- 495 Bentz, B. J., J. Régnière, C. J. Fettig, E. M. Hansen, J. L. Hayes, J. A. Hicke, R. G. Kelsey, J. F. Negrón,  
496 and S. J. Seybold. 2010. Climate Change and Bark Beetles of the Western United States and Canada: Direct  
497 and Indirect Effects. BioScience 60:602–613.
- 498 Berryman, A. A. 1982. Population dynamics of bark beetles. Pages 264–314 in Bark Beetles in North  
499 American Conifers: A System for the Study of Evolutionary Biology.
- 500 Brooks, S. P., and A. Gelman. 1998. General Methods for Monitoring Convergence of Iterative Simulations.  
501 Journal of Computational and Graphical Statistics 7:434.
- 502 Bürkner, P.-C. 2017. **Brms** : An *R* Package for Bayesian Multilevel Models Using *Stan*. Journal of Statistical  
503 Software 80.
- 504 Chubaty, A. M., B. D. Roitberg, and C. Li. 2009. A dynamic host selection model for mountain pine beetle,  
505 *Dendroctonus ponderosae* Hopkins. Ecological Modelling 220:1241–1250.
- 506 Clevers, J., and A. Gitelson. 2013. Remote estimation of crop and grass chlorophyll and nitrogen content using  
507 red-edge bands on Sentinel-2 and -3. International Journal of Applied Earth Observation and Geoinformation  
508 23:344–351.
- 509 Coops, N. C., M. Johnson, M. A. Wulder, and J. C. White. 2006. Assessment of QuickBird high spatial  
510 resolution imagery to detect red attack damage due to mountain pine beetle infestation. Remote Sensing of  
511 Environment 103:67–80.
- 512 DJI. 2015a. Zenmuse X3 - Creativity Unleashed. <https://www.dji.com/zenmuse-x3/info>.
- 513 DJI. 2015b. DJI - The World Leader in Camera Drones/Quadcopters for Aerial Photography. <https://www.dji.com/matrice100/info>.
- 515 DronesMadeEasy. 2018. Map Pilot for DJI on iOS. <https://itunes.apple.com/us/app/map-pilot-for-dji/id1014765000?mt=8>.
- 517 Evenden, M. L., C. M. Whitehouse, and J. Sykes. 2014. Factors Influencing Flight Capacity of the Mountain  
518 Pine Beetle (Coleoptera: Curculionidae: Scolytinae). Environmental Entomology 43:187–196.
- 519 Eysn, L., M. Hollaus, E. Lindberg, F. Berger, J.-M. Monnet, M. Dalponte, M. Kobal, M. Pellegrini, E.

- 520 Lingua, D. Mongus, and N. Pfeifer. 2015. A Benchmark of Lidar-Based Single Tree Detection Methods Using  
521 Heterogeneous Forest Data from the Alpine Space. *Forests* 6:1721–1747.
- 522 Farr, T. G., P. A. Rosen, E. Caro, R. Crippen, R. Duren, S. Hensley, M. Kobrick, M. Paller, E. Rodriguez, L.  
523 Roth, D. Seal, S. Shaffer, J. Shimada, J. Umland, M. Werner, M. Oskin, D. Burbank, and D. Alsdorf. 2007.  
524 The Shuttle Radar Topography Mission. *Reviews of Geophysics* 45.
- 525 Fettig, C. J. 2012. Chapter 2: Forest health and bark beetles. *in* Managing Sierra Nevada Forests. PSW-  
526 GTR-237. USDA Forest Service.
- 527 Fettig, C. J., K. D. Klepzig, R. F. Billings, A. S. Munson, T. E. Nebeker, J. F. Negrón, and J. T. Nowak. 2007.  
528 The effectiveness of vegetation management practices for prevention and control of bark beetle infestations in  
529 coniferous forests of the western and southern United States. *Forest Ecology and Management* 238:24–53.
- 530 Fettig, C. J., L. A. Mortenson, B. M. Bulaon, and P. B. Foulk. 2019. Tree mortality following drought in the  
531 central and southern Sierra Nevada, California, U.S. *Forest Ecology and Management* 432:164–178.
- 532 Flint, L. E., A. L. Flint, J. H. Thorne, and R. Boynton. 2013. Fine-scale hydrologic modeling for regional land-  
533 scape applications: The California Basin Characterization Model development and performance. *Ecological  
534 Processes* 2:25.
- 535 Floyd, M. L., M. Clifford, N. S. Cobb, D. Hanna, R. Delph, P. Ford, and D. Turner. 2009. Relationship of  
536 stand characteristics to drought-induced mortality in three Southwestern piñonJuniper woodlands. *Ecological  
537 Applications* 19:1223–1230.
- 538 Frey, J., K. Kovach, S. Stemmler, and B. Koch. 2018. UAV Photogrammetry of Forests as a Vulnerable  
539 Process. A Sensitivity Analysis for a Structure from Motion RGB-Image Pipeline. *Remote Sensing* 10:912.
- 540 Gabry, J., D. Simpson, A. Vehtari, M. Betancourt, and A. Gelman. 2019. Visualization in Bayesian workflow.  
541 *Journal of the Royal Statistical Society: Series A (Statistics in Society)* 182:389–402.
- 542 Gitelson, A., and M. N. Merzlyak. 1994. Spectral Reflectance Changes Associated with Autumn Senescence  
543 of *Aesculus hippocastanum* L. and *Acer platanoides* L. Leaves. Spectral Features and Relation to Chlorophyll  
544 Estimation. *Journal of Plant Physiology* 143:286–292.
- 545 Graf, M., M. Reid, B. Aukema, and B. Lindgren. 2012. Association of tree diameter with body size and lipid  
546 content of mountain pine beetles. *The Canadian Entomologist* 144:467–477.
- 547 Gray, P. C., A. B. Fleishman, D. J. Klein, M. W. McKown, V. S. Bézy, K. J. Lohmann, and D. W. Johnston.  
548 2019. A convolutional neural network for detecting sea turtles in drone imagery. *Methods in Ecology and*

- 549 Evolution 10:345–355.
- 550 Griffin, D., and K. J. Anchukaitis. 2014. How unusual is the 20122014 California drought? Geophysical  
551 Research Letters 41:9017–9023.
- 552 Hayes, C. J., C. J. Fettig, and L. D. Merrill. 2009. Evaluation of Multiple Funnel Traps and Stand  
553 Characteristics for Estimating Western Pine Beetle-Caused Tree Mortality. Journal of Economic Entomology  
554 102:2170–2182.
- 555 Hijmans, R. J., J. van Etten, M. Sumner, J. Cheng, A. Bevan, R. Bivand, L. Busetto, M. Canty, D. Forrest,  
556 A. Ghosh, D. Golicher, J. Gray, J. A. Greenberg, P. Hiemstra, I. for M. A. Geosciences, C. Karney, M.  
557 Mattiuzzi, S. Mosher, J. Nowosad, E. Pebesma, O. P. Lamigueiro, E. B. Racine, B. Rowlingson, A. Shortridge,  
558 B. Venables, and R. Wueest. 2019. Raster: Geographic Data Analysis and Modeling.
- 559 Hunziker, P. 2017. Velox: Fast Raster Manipulation and Extraction.
- 560 Jakubowski, M. K., W. Li, Q. Guo, and M. Kelly. 2013. Delineating Individual Trees from Lidar Data: A  
561 Comparison of Vector- and Raster-based Segmentation Approaches. Remote Sensing 5:4163–4186.
- 562 Kane, V. R., M. P. North, J. A. Lutz, D. J. Churchill, S. L. Roberts, D. F. Smith, R. J. McGaughey, J. T.  
563 Kane, and M. L. Brooks. 2014. Assessing fire effects on forest spatial structure using a fusion of Landsat and  
564 airborne LiDAR data in Yosemite National Park. Remote Sensing of Environment 151:89–101.
- 565 Kolb, T. E., C. J. Fettig, M. P. Ayres, B. J. Bentz, J. A. Hicke, R. Mathiasen, J. E. Stewart, and A. S. Weed.  
566 2016. Observed and anticipated impacts of drought on forest insects and diseases in the United States. Forest  
567 Ecology and Management 380:321–334.
- 568 Kuhn, M. 2008. Building Predictive Models in R Using the caret Package. Journal of Statistical Software  
569 28:1–26.
- 570 Larson, A. J., and D. Churchill. 2012. Tree spatial patterns in fire-frequent forests of western North America,  
571 including mechanisms of pattern formation and implications for designing fuel reduction and restoration  
572 treatments. Forest Ecology and Management 267:74–92.
- 573 Li, W., Q. Guo, M. K. Jakubowski, and M. Kelly. 2012. A New Method for Segmenting Individual Trees  
574 from the Lidar Point Cloud. Photogrammetric Engineering & Remote Sensing 78:75–84.
- 575 Logan, J. A., P. White, B. J. Bentz, and J. A. Powell. 1998. Model Analysis of Spatial Patterns in Mountain  
576 Pine Beetle Outbreaks. Theoretical Population Biology 53:236–255.
- 577 Meyer, F., and S. Beucher. 1990. Morphological segmentation. Journal of Visual Communication and Image

- 578 Representation 1:21–46.
- 579 Micasense. 2015. MicaSense. <https://support.micasense.com/hc/en-us/articles/215261448-RedEdge-User-Manual-PDF-Download>
- 580 Millar, C. I., R. D. Westfall, D. L. Delany, M. J. Bokach, A. L. Flint, and L. E. Flint. 2012. Forest  
581 mortality in high-elevation whitebark pine (*Pinus Albicaulis*) forests of eastern California, USA; influence  
582 of environmental context, bark beetles, climatic water deficit, and warming. Canadian Journal of Forest  
583 Research 42:749–765.
- 584 Miller, J. M., and F. P. Keen. 1960. Biology and control of the western pine beetle: A summary of the first  
585 fifty years of research. US Department of Agriculture.
- 586 Moeck, H. A., D. L. Wood, and K. Q. Lindahl. 1981. Host selection behavior of bark beetles (Coleoptera:  
587 Scolytidae) attacking *Pinus ponderosa*, with special emphasis on the western pine beetle, *Dendroctonus*  
588 *brevicomis*. Journal of Chemical Ecology 7:49–83.
- 589 Morris, J. L., S. Cottrell, C. J. Fettig, W. D. Hansen, R. L. Sherriff, V. A. Carter, J. L. Clear, J. Clement, R.  
590 J. DeRose, J. A. Hicke, P. E. Higuera, K. M. Mattor, A. W. R. Seddon, H. T. Seppä, J. D. Stednick, and S.  
591 J. Seybold. 2017. Managing bark beetle impacts on ecosystems and society: Priority questions to motivate  
592 future research. Journal of Applied Ecology 54:750–760.
- 593 North, M. P., S. L. Stephens, B. M. Collins, J. K. Agee, G. Aplet, J. F. Franklin, and P. Z. Fule. 2015.  
594 Reform forest fire management. Science 349:1280–1281.
- 595 Pau, G., F. Fuchs, O. Sklyar, M. Boutros, and W. Huber. 2010. EBImagean R package for image processing  
596 with applications to cellular phenotypes. Bioinformatics 26:979–981.
- 597 Pebesma, E., R. Bivand, E. Racine, M. Sumner, I. Cook, T. Keitt, R. Lovelace, H. Wickham, J. Ooms, K.  
598 Müller, and T. L. Pedersen. 2019. Sf: Simple Features for R.
- 599 Pile, L. S., M. D. Meyer, R. Rojas, O. Roe, and M. T. Smith. 2019. Drought Impacts and Compounding  
600 Mortality on Forest Trees in the Southern Sierra Nevada. Forests 10:237.
- 601 Plowright, A. 2018. ForestTools: Analyzing Remotely Sensed Forest Data.
- 602 Popescu, S. C., and R. H. Wynne. 2004. Seeing the Trees in the Forest: Using Lidar and Multispectral Data  
603 Fusion with Local Filtering and Variable Window Size for Estimating Tree Height. PHOTOGRAMMETRIC  
604 ENGINEERING:16.
- 605 Preisler, H. K., N. E. Grulke, Z. Heath, and S. L. Smith. 2017. Analysis and out-year forecast of beetle,  
606 borer, and drought-induced tree mortality in California. Forest Ecology and Management. 399: 166-178

- 607 399:166–178.
- 608 R Core Team. 2018. R: A Language and Environment for Statistical Computing. R Foundation for Statistical  
609 Computing, Vienna, Austria.
- 610 Raffa, K. F., and A. A. Berryman. 1983. The Role of Host Plant Resistance in the Colonization Behavior  
611 and Ecology of Bark Beetles (Coleoptera: Scolytidae). Ecological Monographs 53:27–49.
- 612 Raffa, K. F., and A. A. Berryman. 1987. Interacting Selective Pressures in Conifer-Bark Beetle Systems: A  
613 Basis for Reciprocal Adaptations? The American Naturalist 129:234–262.
- 614 Raffa, K. F., B. H. Aukema, B. J. Bentz, A. L. Carroll, J. A. Hicke, M. G. Turner, and W. H. Romme. 2008.  
615 Cross-scale Drivers of Natural Disturbances Prone to Anthropogenic Amplification: The Dynamics of Bark  
616 Beetle Eruptions. BioScience 58:501–517.
- 617 Raffa, K. F., J.-C. Grégoire, and B. Staffan Lindgren. 2015. Natural History and Ecology of Bark Beetles.  
618 Pages 1–40 in Bark Beetles. Elsevier.
- 619 Rouse, W., R. H. Haas, W. Deering, and J. A. Schell. 1973. MONITORING THE VERNAL ADVANCEMENT  
620 AND RETROGRADATION (GREEN WAVE EFFECT) OF NATURAL VEGETATION. Type II Report,  
621 Goddard Space Flight Center, Greenbelt, MD, USA.
- 622 Roussel, J.-R. 2019. lidRplugins: Extra functions and algorithms for lidR package.
- 623 Roussel, J.-R., D. A. (. the documentation), F. D. B. (. bugs and improved catalog features), and A. S. M. (.  
624 lassnags). 2019. lidR: Airborne LiDAR Data Manipulation and Visualization for Forestry Applications.
- 625 Seidl, R., J. Müller, T. Hothorn, C. Bässler, M. Heurich, and M. Kautz. 2016. Small beetle, large-scale  
626 drivers: How regional and landscape factors affect outbreaks of the European spruce bark beetle. The Journal  
627 of applied ecology 53:530–540.
- 628 Shiklomanov, A. N., B. A. Bradley, K. M. Dahlin, A. M. Fox, C. M. Gough, F. M. Hoffman, E. M. Middleton,  
629 S. P. Serbin, L. Smallman, and W. K. Smith. 2019. Enhancing global change experiments through integration  
630 of remote-sensing techniques. Frontiers in Ecology and the Environment 0.
- 631 Shin, P., T. Sankey, M. Moore, and A. Thode. 2018. Evaluating Unmanned Aerial Vehicle Images for  
632 Estimating Forest Canopy Fuels in a Ponderosa Pine Stand. Remote Sensing 10:1266.
- 633 Stephenson, N. 1998. Actual evapotranspiration and deficit: Biologically meaningful correlates of vegetation  
634 distribution across spatial scales. Journal of Biogeography 25:855–870.
- 635 Stephenson, N. L., A. J. Das, N. J. Ampersee, and B. M. Bulaon. 2019. Which trees die during drought?

- 636 The key role of insect host-tree selection. *Journal of Ecology*:75.
- 637 Thistle, H. W., H. Peterson, G. Allwine, B. Lamb, T. Strand, E. H. Holsten, and P. J. Shea. 2004. Surrogate  
638 Pheromone Plumes in Three Forest Trunk Spaces: Composite Statistics and Case Studies. *Forest Science* 50.
- 639 USDAFS. 2019, February 11. Press Release: Survey finds 18 million trees died in California in 2018.  
640 [https://www.fs.usda.gov/Internet/FSE\\_DOCUMENTS/FSEPRD609321.pdf](https://www.fs.usda.gov/Internet/FSE_DOCUMENTS/FSEPRD609321.pdf).
- 641 Vega, C., A. Hamrouni, S. El Mokhtari, J. Morel, J. Bock, J. P. Renaud, M. Bouvier, and S. Durrieu. 2014.  
642 PTrees: A point-based approach to forest tree extraction from lidar data. *International Journal of Applied  
643 Earth Observation and Geoinformation* 33:98–108.
- 644 White, P., and J. Powell. 1997. Phase transition from environmental to dynamic determinism in mountain  
645 pine beetle attack. *Bulletin of Mathematical Biology* 59:609–643.
- 646 Young, D. J. N., J. T. Stevens, J. M. Earles, J. Moore, A. Ellis, A. L. Jirka, and A. M. Latimer. 2017.  
647 Long-term climate and competition explain forest mortality patterns under extreme drought. *Ecology Letters*  
648 20:78–86.
- 649 Zhang, W., J. Qi, P. Wan, H. Wang, D. Xie, X. Wang, and G. Yan. 2016. An Easy-to-Use Airborne LiDAR  
650 Data Filtering Method Based on Cloth Simulation. *Remote Sensing* 8:501.